Journal of The
Electrochemical Society

A Segmented Along the Channel Test Cell for Locally Resolved Analysis at High Current Densities in PEM Water Electrolysis

To cite this article: Niklas Hensle *et al* 2024 *J. Electrochem. Soc.* **171** 114510

Journal of The Electrochemical Society, 2024 **171** 114510

A Segmented Along the Channel Test Cell for Locally Resolved Analysis at High Current Densities in PEM Water Electrolysis

Niklas Hensle,[1,2,z] Sebastian Metz,[1] André Weber,[2] and Tom Smolinka[1]

[1]*Fraunhofer Institute for Solar Energy Systems ISE, Heidenhofstrasse 2, 79110, Freiburg, Germany*
[2]*Institute for Applied Materials (IAM-ET), Karlsruhe Institute of Technology (KIT), Adenauerring 20b, 76131, Karlsruhe, Germany*

For the scale-up of proton exchange membrane (PEM) water electrolysis, understanding the cell behavior on industrial scale is a prerequisite. A proper distribution of current and temperature in the cell can improve performance and decrease overall degradation effects. Due to water consumption as well as the concomitant gas evolution and accumulation, gradients and inhomogeneities along the reaction coordinate are expected. These effects increase along the water supply channels of a flow field and are expected to lead to spatial gradients in cell performance and temperature. In this study we present a new test cell that is segmented along the flow field channels and is designed for the operation at high current densities. We show polarization curve measurements at 10 bar differential pressure up to 10 A·cm^{-2} at ∼2.7 V without observing any mass transport limitations and conduct current density, temperature and impedance distribution measurements. At harsh conditions (low water flow rates of 2 ml·min^{-1}·cm^{-2} and high current densities up to 6 A·cm^{-2}) we see significant temperature and current density increase of ∼13 K and 0.7 A·cm^{-2} which can be explained by decreasing membrane resistance determined via EIS of >10 mΩ·cm^2 along the channel. The validity of the impedance measurements is proofed by comparison of the impedance at 100 mHz with the direct current resistance of the cell extracted by the local slope of the polarization curve.

Manuscript submitted July 29, 2024; revised manuscript received October 29, 2024. Published November 19, 2024.

Supplementary material for this article is available online

Industrial proton exchange membrane (PEM) water electrolysis stacks with cell areas of several 1,000 cm^2 require a proper water and heat distribution to reduce local degradation and increase the overall stack performance.[1–6] PEM water electrolysis laboratory test cells with an industrially relevant cell length allow the investigation of problems due to the consumption of reactant water and accumulation of the produced gas along the channel. The latter can lead to current density and temperature inhomogeneities and therefore imposes local stress on the components.[3,7–9] Furthermore, the gas accumulation is challenging for a proper transport of water to and in the porous electrode and can increase mass transport losses (MTL).[10,11]

These issues get even more pressing with the expected future reduction of the total cell resistance. With a drastic reduction of ohmic resistances, for example by using thinner proton exchange membranes, current densities >3 A·cm^{-2} are feasible.[12] The development targets of *Clean Hydrogen Partnership*, European Union and the *U.S. Department of Energy*, USA define an electricity consumption for electrolysis systems including balance of plant at nominal capacity of 48 kWh·kg^{-1} and 46 kWh·kg^{-1} for the year 2030 (EU) and 2026 (USA), respectively.[13] These targets are only feasible by increasing the current density and cell efficiency drastically, targeting 1.75 V cell voltage, which meets $\eta_{HHV} > 84$ % (HHV, higher heating value), at an average current density of 3.5 A·cm^{-2}.[14] At high current densities and at low stoichiometric reactant supply mass transport processes tend to become dominant since the charge transfer resistance is decreasing and diffusion overpotentials are increasing with increasing gas production. The water consumption and gas accumulation along channels with an industrially relevant length can lead to even higher diffusion and mass transport problems when operating at stoichiometric water supply. However, current publications do not focus on analyzing electrochemical processes at high current densities. Only few publications are facing current densities out of the scope of today's industrial standard (>3 A·cm^{-2}).[12,15–17]

In our previous work we could show further that with increasing current densities, besides conventional mass transport processes, a yet unclear process is observable, which appears as an inductive loop in impedance spectra.[18] This process that was discussed for other electrochemical applications like batteries and fuel cells,[19–23] is favorable as it decreases the direct current (DC) resistance of the cell.

To investigate these phenomena along the water supply channels, locally resolved measurements can be used to analyze the distribution of current density, temperature and electrochemical impedance.[8] Focusing on the cell behavior in the flow dimension only, an *along the channel* approach can be used. For this purpose, test cells are designed at laboratory scale with cell widths of a few centimeters and an industrial scale in the cell length (30 cm and longer). The test cells are usually divided into segments along the water-gas channels with an electrical disconnection between each segment to increase the measurements selectivity and decrease in-plane crosstalk. This analysis method is well-established for PEM fuel cells for which most of the work focusses on current density distribution (CDD) measurements.[24–30] Also some publications on locally resolved impedance investigations are reported.[31–33] While in the PEM water electrolysis this setup has not been used equally much some studies are published on CDD,[1,2,4,9,34] temperature distribution[3,8] and locally resolved impedance measurements.[3,7]

Immerz et al. presented a 50 × 0.5 cm^2 segmented single-channel PEM water electrolysis test cell with highly resolved current and temperature monitoring.[7,8] Additionally, sequential electrochemical impedance spectroscopy (EIS) can be conducted at the inlet, the center and the outlet of the cell to gain information about the series resistance as well as charge transfer and mass transport processes. They observed an increase of the high frequency series resistance (HFR), mass transport polarization resistance and therefore decreasing current towards the cell outlet under water starvation of the cell. Furthermore, for the first time, they discussed current density inhomogeneities and their origin in a segmented along the channel cell. However, the cell operation was at rather low current densities of <1.5 A·cm^{-2}.

Parra-Restrepo et al. presented a 30 × 1 cm^2 multi-channel PEM water electrolysis test cell which is divided into 20 segments.[9] This cell is meant to measure the current density and impedance distribution along the channel. Furthermore, a parallel channel fed

[z]E-mail: niklas.hensle@ise.fraunhofer.de

with hydrogen is added to implement a reference electrode for each segment. The cell was also used for fuel cell operation for which EIS results are published.[32] For the electrolysis mode, only current density distribution results were published. They analyzed PTLs varying in pore size and could see a significant influence on mass transport up to a current density of 3.5 A·cm^{-2}.

Sun et al. presented a circular shaped test cell with an active area of 49.5 cm^2 divided into 11 segments and measured the current density and impedance distribution up to 0.8 A·cm^{-2}. They could observe that with a water stoichiometry of less than 5 the current density is extremely influenced which leads to a decrease of current along the flow channels. For higher water stoichiometry a rather stable current distribution was measured. They could correlate the current density behavior at different water stoichiometry with the increasing HFR towards the cell outlet which might be concluded as membrane dry out.

Dedigama et al. provided a 0.3 × 8.5 cm^2 single-channel test cell with the possibility to measure the current density distribution and visualize the bubble behavior due to use of transparent components in the end plate.[34] They showed a significant increase of the current density towards the cell outlet. Compared to the publications mentioned above the water stoichiometry used here is significantly higher (water stoichiometry $>$ 100) which might explain the increasing current density towards the end of the cell due to an increasing temperature and a lack of water supply issues. With the bubble visualization they observed large bubbles towards the cell outlet most likely related to gas accumulation along the flow channel and the higher gas production due to the increased current density at the cell outlet. However, the current density here was as well very low with a maximum of 0.5 A·cm^{-2}.

In this contribution we present a segmented along the channel (AtC) PEM water electrolysis cell that enables spatially resolved current density, temperature and impedance measurements. We show results on current density and temperature distribution and locally resolved impedance spectroscopy for high current densities of up to 10 A·cm^{-2} and 10 bar differential pressure. With this approach it is possible to analyze inhomogeneities and gradients along industrial-relevant channels for the first of its kind at current and future industrial operation. At high current densities in combination with low water flow rates we detect large temperature gradients between the cell inlet and outlet of more than 10 K, which leads to higher current densities at the cell outlet. Using local impedance analysis we can refer this to decreasing membrane resistance. The dominant impact of temperature seems to fully compensate dry-out effects at these water flow rates, membrane dry-out seems to be only relevant when operating close to the stoichiometric water amount as shown in.[7] To validate the impedance measurement, we compare the impedance at low frequencies (100 mHz) of the mean cell and the cell segments with the direct current resistance which is extracted by the local slope of polarization curve measurements. With this test cell, we can provide relevant information about local phenomena occurring and recommendations on cell dimensioning and operation in industrial scale.

Experimental

The AtC test cell presented here has an active area of 60 cm^2 with a length of 30 cm and a width of 2 cm. Herewith, the cell represents the lower limit of industrial cell and channel lengths. It is designed for a current density of up to 10 A·cm^{-2} (600 A absolute). The cell can be operated under pressure of up to 30 bar and was so far successfully tested at up to 10 bar differential and balanced pressure. The temperature can be varied between 40°C and 80°C and flow rates up to 2000 ml·min^{-1} can be achieved.

For locally resolved electrochemical characterization EIS can be performed in 10 segments plus the whole cell in parallel. Additional to this, 120 sensors are contacted to the flow field plate (monopolar plate) to measure the current density and temperature distribution. With this cell design, it is possible to segment the flow field plate and the porous transport layers (PTL) separately from each other. Therefore, both or only one half-cell can be segmented. The default combination in this study is the segmentation of the flow field plate and the PTL at the anode and to use an unsegmented flow field plate and PTLs at the cathode.

Cell setup.—An overview of the cell design and its components is given in Fig. 1. Figure 1a shows an exploded-view drawing of the default setup with segmented flow field plate at the anode side (bottom) and unsegmented flow field plate at the cathode side (top). The components numbered in Fig. 1a and discussed below are summed up in Table I with a short description. Additionally, photos taken during the assembly of the cell and of the assembled cell implemented in the test bench are given in the Supplementary Information SI1.

The cell consists of different cell components which are placed on top of each other and compressed together to ensure gas tightness and a proper electrical contact. For the compression a pneumatic clamping pressure system (1) was designed. Hereby, a moveable stamp at the bottom of the cell compresses all stacked components against the counter plate (2) on top. Spring discs on top of the counter plate are used to equalize the clamping pressure distribution.

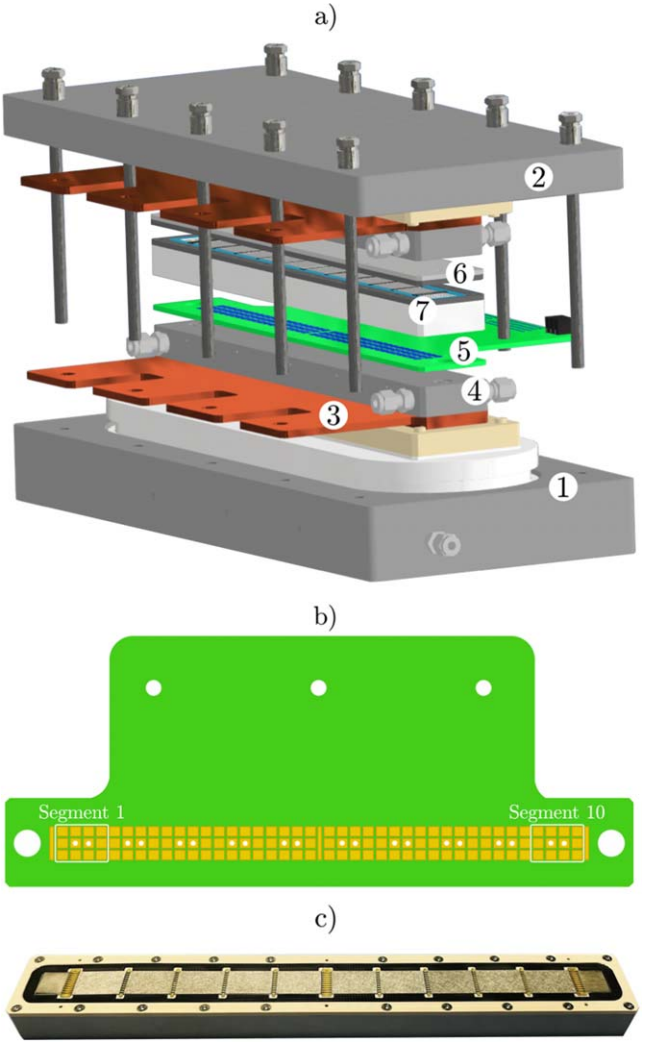

Figure 1. (a) Exploded-view drawing of the AtC cell (for numbering see description in the section cell setup) with default setup (anode segmented, cathode unsegmented), (b) top view on the printed-circuit board and (c) segmented flow field plate with inserted PTLs.

Table I. Overview and short description of the cell components of the AtC cell shown in Fig. 1a.

No	Name	Functionality	Materials used
(1)	Clamping pressure system	Pneumatic compression of the cell components	High-strength aluminium
(2)	Counter plate	Fixed bearing for compression	High-strength aluminium
(3)	Current collector	Current interface between current cables and homogenization plate (4)	Gold-coated copper
(4)	Homogenization plate	Transfer current and fluidics to and from flow field plate	Titanium grade 2
(5)	Printed circuit board (PCB)	Locally resolved measurements of current, temperature and impedance	Gold-coated copper contacts embedded in FR-4 epoxy
(6)	Unsegmented flow field plate	Electrically uninsulated cathode flow field plate	Gold-coated titanium grade 2
(7)	Segmented flow field plate	Electrically segmented anode flow field plate	Gold-coated titanium grade 2 with non-conductive frame

To pass the current through the cell, gold coated current collector plates (3) made from copper are implemented at anode and cathode. Each current collector plate is electrically insulated against the clamping pressure system using polymer plates. Two 120 mm^2 copper cables are used per pole to transfer the current (up to 600 A) from the power supply to the cell. At each side a 20 mm thick homogenization plate (4) made from titanium is placed at the inner side of the current collector to transfer the current towards the active area of the cell and to homogenize transverse currents and set the boundary cell components onto an equal potential. Additional to this, the water inlets and water-gas outlets are integrated to these titanium plates.

For the locally resolved measurements, a printed circuit board (PCB) (5) custom-designed by *DiLiCo engineering GmbH*, Germany is implemented between the homogenization plate and the flow field plate at one of the half-cells. The PCB consists of 40 measurement contacts along the channel in three columns resulting in a total of 120 contacts. The cell is divided by the flow field plate and the PTLs in 10 equal segments, per segment 4×3 contacts are available, exemplarily highlighted for segment 1 and 10 in Fig. 1b. For each contact the current density is determined via a shunt resistor. The 12 measurement contacts per segment are interconnected using soft conductive material to ensure that very similar current is flowing through the shunts within one segment.

Per segment at the two centered measurement contacts of the 12 shunts per segment (highlighted with white dots in Fig. 1b) the alternating current (AC) potential for EIS analysis is measured using a frequency response analyzer (FRA) by *Zahner-Elektrik GmbH & Co. KG*, Germany before and after the shunt resistor to gain information on the local AC current, see Fig. 2. With this set up it is possible to measure the impedance at each segment in parallel.

Additional to this, in a second layer 120 Pt100 sensors are implemented in the PCB to monitor the temperature distribution. At the inlet, center and outlet potential measurements can be done, see longer vertical contacts in Fig. 1b, to connect reference electrodes using a laser ablation approach[35] which are not discussed within this work. Detailed information about the measurement technique is provided in section *Measurement method*.

Upon the PCB at the anode and upon the homogenization plate at the cathode the titanium flow field plate is placed. The flow field plate has 10 milled parallel supply channels, each with a cross sectional width of 1 mm and a depth of 2 mm. For the unsegmented flow field plate (6) at the cathode, a solid titanium plate was manufactured. For the segmented flow field plate (7) at the anode, 10 titanium inlets with an active contact area of 20×28 mm^2 are pressed into an electrically insulating frame sealed using two radial O-ring gaskets. Figure 1c shows the assembled segmented flow field plate with inserted PTLs. The flow field plates are gold coated to minimize corrosion and contact resistances, see the channels at inlet, center and outlet at the positions of the (not used) reference electrodes. The segmented flow field plate has a height of 23 mm. To be flexible in using PTLs with different thicknesses polymer frames with different heights are screwed upon the flow field plate. Between the flow field plate and the frame, as well as on top of the frame a flat sealing by *Freudenberg FST GmbH*, Germany is used.

On top of the flow field plate, the PTLs are placed. To segment the PTLs, they are shaped into 20×28 mm^2 pieces and insulating bridges with 2 mm width are inserted. The insulating bridges are designed to avoid electrical contact between the PTL and to affect the water flow in the flow channels only marginally. Between the two flow field plates with inserted PTLs and flat sealings the CCM is positioned. The active area of the segmented cell setup is determined by the area of all 10 segments resulting in 56 cm^2.

A commercial E400 Gen. 3 CCM by *Greenerity GmbH*, Germany with a 125 μm thick Nafion®-based membrane is employed in this study. At the anode PTLs with a thickness of 500 μm (2GDL20–0.5) by *NV Bekaert SA*, Belgium which were in-house sputter-coated with 100 nm platinum on both sides are employed. At the cathode, a carbon-based gas diffusion layer (GDL) with a thickness of 215 μm (SGL 22 BB) by *SGL Carbon SE*, Germany is used.

Measurement method.—A schematic cross-section view of the active parts of the AtC test cell and its technique for current density, temperature and impedance distribution measurements are shown in Fig. 2. The PCB is positioned between the homogenization plate and the flow field plate at the anode, more detailed information on the used PCB system by the supplier is provided elsewhere.[26]

The current density distribution of the DC-bias is determined by measuring the potential difference with a four-wire setup before ($\varphi_{DC,cell}$) and after ($\varphi_{DC,end}$) the implemented shunt resistors with $R = 33$ mΩ resistance, see Fig. 2c. The measurement accuracy tested by the supplier is for small currents <50 mA per shunt ± 0.1 mA. For the whole current density range used within this study (up to 5 A per shunt) $\pm 1\%$ measurement accuracy is guaranteed. According to Ohm's law the current is determined by measuring the voltage drop over the known resistance of the shunt resistor.

The temperature distribution is determined by using Pt100 sensors at the same positions as the current density measurement as well with a four-wire setup.

For the locally resolved EIS, one of the two centered shunt resistors per segment is used. Soft conductive GDL material is placed between the PCB and the flow field segment to electrically connect the 12 shunts per segment together. Since the standard deviation of the current within one segment (measured using the 12 shunts) is $<0.5\%$, one shunt properly represents the EIS for the whole segment. The supporting GDLs between PCB and flow field plate per segment do not have any contact to surrounding segments. The active area for one shunt resistor is calculated by the active area of the whole cell divided by the 120 contacts. The measurement technique is visualized in Fig. 2a for the overall cell voltage and in Fig. 2c for the local current measurement during EIS.

For the cell operation a potentiostat and FRA system by *Zahner Elektrik GmbH & Co. KG*, Germany is used. The potentiostat system consisting of *Zahner Zennium X* and *Zahner EL1000* is implemented into the test bench. With an additional third-party power source by

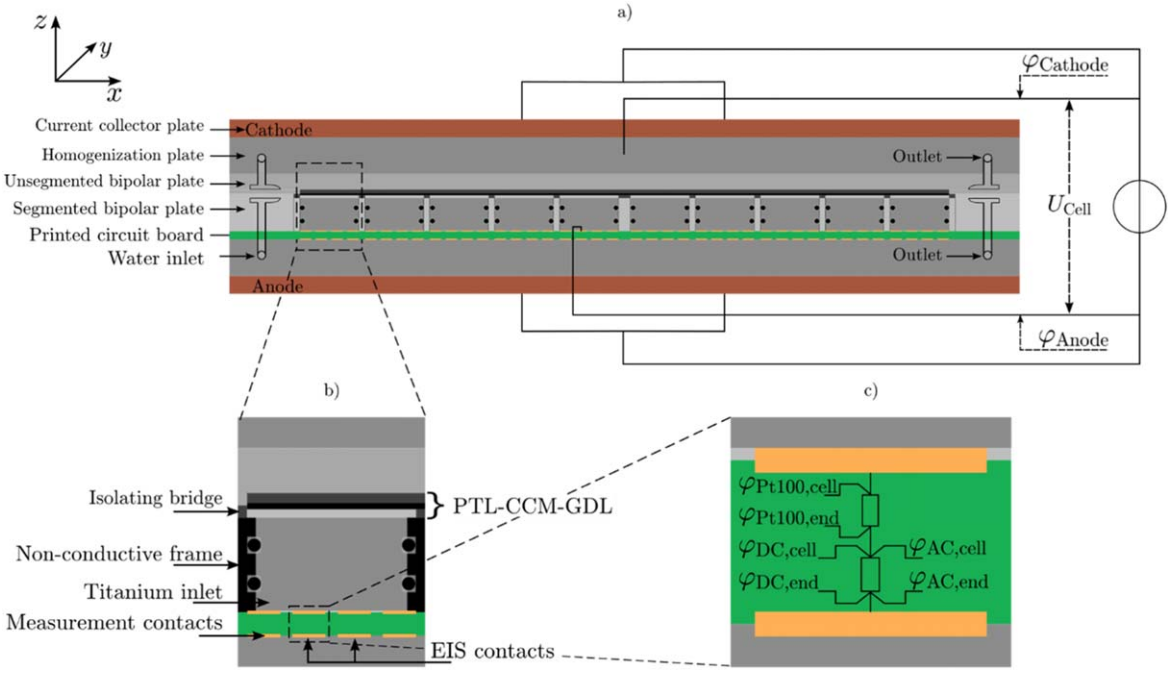

Figure 2. (a) Schematic cross-section of the AtC test cell, (b) detailed presentation of segment 1 and (c) explanation of current density, impedance and temperature measurement representative at one of the 120 measurement contacts.

TDK Lambda, Germany DC currents up to 680 A can be reached. Details about the electrical connection of the Zahner and the power source can be found at.[36] To set a DC-bias the current cables are contacted to the current collector plates at anode and cathode. At the opposite side of the cell, the cell potential (DC and AC) is measured using the main channel of *Zahner EL1000*. At the non-segmented half-cell, the sense wires are connected to the homogenization plate which is directly contacted to the flow field plate, see Fig. 1a. At the half-cell with implemented PCB the potential is measured between the flow field plate and the shunt resistor in segment 5 to exclude the shunt resistance in the cell voltage measurement, see Fig. 2a.

The additional sense wires of *Zahner Zennium X* are connected before ($\varphi_{AC,cell}$) and after ($\varphi_{AC,end}$) the shunt resistors in the PCB, analogously to the DC measurement, see Fig. 2c. For the data recording, the parallel voltage measurement cards (*Zahner PAD 4*) with a voltage range of ±1V are employed. With the calibrated resistance of the shunt resistor the local current during the EIS can be determined by measuring the voltage drop, analogously to the DC measurement. This is done at one shunt resistor per segment resulting in a total measurement of 10 segments and the mean cell in parallel. To determine the local impedance the voltage measurement of the mean cell is then used referring to each segment and the whole cell current measurements. This implies the assumption of very equal voltage along the channel, which is discussed in the *Results and Discussion* section. With this measurement setup, it is possible to operate the cell either in potentiostatic or in galvanostatic mode; all results presented here were obtained in galvanostatic mode.

Test bench.—The test bench used within this work is an in-house built test bench at *Fraunhofer ISE*[10] which was modified for the operation at high currents. The test bench is designed up to 1000 A (DC) and 10 V, pressure of 50 bar, temperature of 80 °C and a flow rate of up to 2 l·min^{-1}. The water flow at anode and cathode can be circulated independently and the water quality is controlled. The two-phase flow coming out of the test cell is fed in a gas water separator whereby the water is recovered, and the gases leave the test bench through the exhaust. Inline ion exchangers to guarantee a low conductivity of the recirculated water at anode and cathode are employed. A water quality of $<0.1\,\mu S\ cm^{-1}$ is assured during measurements independently of the applied temperature and pressure. The test bench is controlled using an inhouse developed LabVIEW software environment by *National Instruments*, USA. This includes pressure and temperature, which are measured and controlled at the cell inlet or outlet, as well as the water inlet flow. The impedance measurements are done with a current amplitude of 10% of the DC-bias between frequencies of 10 kHz and 100 mHz with 10 measurement points per decade and an integration time corresponding to 10 periods. The measurements are proofed on drift and non-linearities using the Kramers-Kronig test.[37] The criterion of a valid measurement was set to Kramers-Kronig residuals of less than 1% at each frequency point. All impedance spectra shown in this study fulfill the Kramers-Kronig test.

Results and Discussion

This section provides in situ measurement results with the aim to discuss the quality of the present AtC cell regarding the internal contacting of the segments, the proof of the voltage equality along the channel, the HFR analysis (see Supplementary Information SI3) and the consistency between locally resolved DC-measurements and EIS at different operational conditions. An overview of the results with the main outcome and short discussion is given in the Supplementary Information Table SI7.

Internal contact distribution.—An evenly distributed contacting of the segments is essential to analyze along the channel effects in the cell. Without proper contacting an externally induced current distribution can occur which falsifies the measurement results. Unfortunately, a perfect contacting is impossible, therefore the deviations must be considered in our data analysis. C. Immerz et al. reported an influence of PTL and CCM material which led to a current density deviation up to 30% compared to the mean value. With a current density distribution measurement at a low mean current density a reference profile was measured. At different operation points the deviation to the reference profile was calculated and the changes analyzed.[8]

In the here presented setup, three main issues can lead to current density inhomogeneities: (1) component tolerance, like PTL and

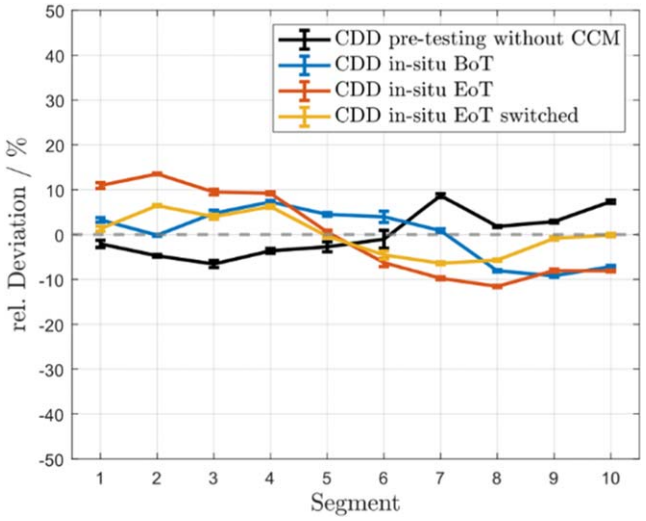

Figure 3. Analysis of the internal contacting of the segments by measuring the current density distribution (CDD). Relative deviation of pre-testing and in situ tests at BoT, EoT and with switched water inlet and outlet. The current applied is 5 A in total. In-situ measurements are done at 80 °C and 10 ml·min^{-1}·cm^{-2}, pre-testing at dry conditions and room temperature.

CCM material but also of all milled components and the PCB; (2) global bending of the counter plate and (3) local contacting issues to the measurement contacts of the PCB. To equalize production tolerances, soft conductive material is employed. Small pieces of carbon-based GDL material are used between the flow plate and the PCB to improve the contacting. Influence of global bending of the counter plate has been minimized by supporting the center of the cell between current collector and counter plate with thin stainless-steel sheets with thicknesses in micrometer scale.

To analyze the influence by uneven contacting, tests with pressure paper by *Fujifilm, Japan* have been performed. Furthermore, before each in situ measurement the test cell is assembled without CCM but with inserted PTLs to measure the current density distribution in dry condition and at room temperature. Applying all optimizations mentioned above the electrical contacting homogeneity (without CCM) could be improved from >35% standard deviation to <5% from the mean current density (5 A absolute) applied, see Supplementary Information SI 2. As a result, the global bending effects and the contacting issues within the segment (reduction of error bar) could be reduced to a minimum.

Furthermore, before and after each electrochemical characterization a CDD reference profile with anodic water flow from segment 1 to 10 and vice-versa is measured with a conditioned cell at begin of test (BoT) and end of test (EoT). Therefore, an operation point at which minimal along the channel effects are expected is chosen (high water flow rate of 10 ml·min^{-1}·cm^{-2} and low current of 5 A absolute at 80 °C). A summary of these pre-tests is given in Fig. 3. Between the pre-testing without CCM and the in situ operation a clear difference can be seen with randomly changing current density distribution. This might be influenced by the CCM and its swelling and the temperature effect on all components. Also, it is to be mentioned that between the pre-testing and the in situ measurement the GDL at the cathode is exchanged to first compress a pristine GDL with the CCM which might have a significant influence as well.

Moreover, the current distribution during the measurement is changing, as we compare the difference between BoT and EoT measurements and the switch of the water inlet has a slight levelling effect on the distribution, see in Fig. 3. However, all CDD profiles have comparable small overall deviations and no clear trend along the channel. Nevertheless, this behavior of the AtC cell during operation needs to be considered in each analysis as it could superimpose important findings.

Voltage equality along the channel.—For the locally resolved measurement method used within this work, it is assumed that the potential of all segments is approximately equal along the channel. To proof this, we measured the mean cell voltage and the impedance in galvanostatic mode at the same position at the cathode but varied the contacted segment (segment 1 to 10) excluding the shunt resistor at the anode. The results are shown in Fig. 4.

We observed a voltage deviation of less than ±0.6% when contacting the different segments, see Fig. 4a which is an excellent proof of the potential equalization in the cell. For different used segments very comparable mean cell impedance and phase angle could be measured without any tendency along the channel, see Fig. 4b. The mean value of the relative standard deviation of impedance and phase angle over the measured frequency range is <1.3% and <3.1%, respectively. We therefore demonstrate that the voltage measurement is independent of the segment in the cell at which the voltage measurement is done and that the assumption of equal voltage distribution along the channel is valid. For completeness it should be mentioned that this voltage deviation test was conducted with a slightly different approach to equalize the contacting of the segments compared with the final setup used throughout the rest of this study, which led to increased ohmic resistance, detectable at the quite high values for the HFR. Under these conditions and improved contacting, we expect a HFR of ~160 mΩ·cm^2, see Fig. 7a.

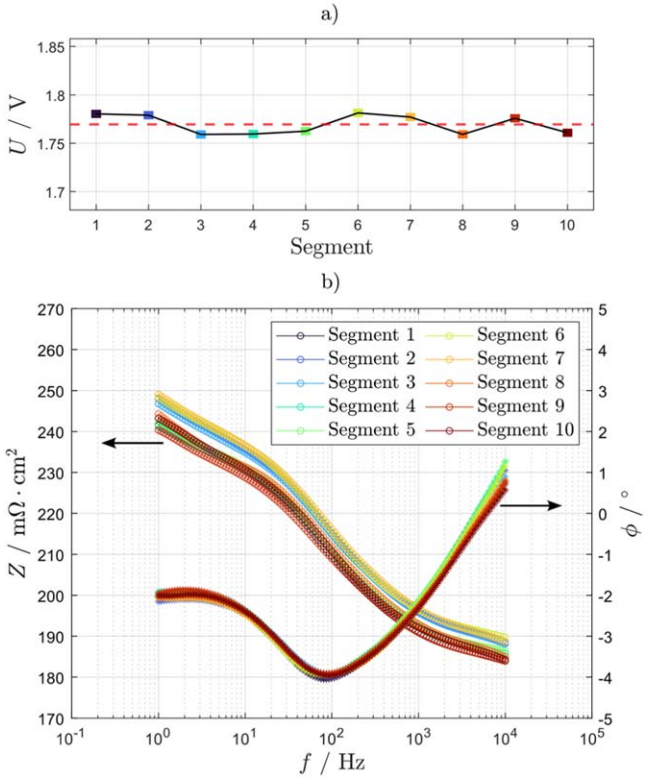

Figure 4. (a) Galvanostatic mean cell voltage measurement and (b) Bode presentation of the mean cell impedance with sense measurement at segment 1 to 10 at the anode. The measurements are done at 60 °C, ambient pressure, 1 A·cm^{-2} and water flow rate at the anode of 10 ml·min^{-1}·cm^{-2}.

Validity of the AtC cell under different operational conditions.—To confirm a good technical performance of the AtC cell and demonstrate that it is fit for purpose to be used in further investigations, we analyzed the overall and local DC performance and impedance under different conditions. We particularly focused on measurements at equal pressure of 1 barg and differential pressure of 10 barg (10 barg cathode, 1 barg anode) at current densities of up to 10 A·cm^{-2}, summarized in Fig. 5.

Figure 5a shows the mean polarization curve of the cell (segment 1 to 10) for both pressure operations up to 10 A·cm^{-2} at 80 °C. The error bars show the deviation of the mean value of the current density and voltage measurement during the last 30 s of each current density step of this measurement. Uncertainties as influences of contacting of the segments (see discussion above), stability issues due to bubble formation and inaccuracies of all control and measurement variables of the test cell and the test bench need to be considered when analyzing these results. Since an exact determination of all possible errors during these measurements is very challenging, reproducibility measurements can deliver a range of expected accuracy.

The reproducibility of the AtC cell was tested by conducting the measurements twice with a new assembly of the cell between the reproducibility measurements. They revealed a voltage deviation of less than 1.4% for the whole current density range even in the most critical operation point regarding reproducibility (10 bar differential pressure). This should be representative for all measurements conducted in this study, see Supplementary Information SI4a).

A high anode water flow rate of 20 ml·min^{-1}·cm^{-2} is chosen to enable minimal temperature gradients along the channel. In both cases, there is no indication for mass transport limitations (exponential trend of the curve towards high current densities). Instead, the curves show a decrease of the slope towards high current densities which is commonly associated to a decrease of the membrane resistance due to a temperature increase.[38] In our previous work we discussed already that temperature effects alone cannot explain this behavior. Instead an increasing inductive loop at low frequencies with increasing current density contributes to a significant decrease in impedance as well.[18]

At low current densities <1 A·cm^{-2} the influence of higher partial pressure of hydrogen resulting in higher voltages can be seen and explained by the pressure dependency of the Nernst equation.[39,40] In summary, only very small differences are observable for the selected operating conditions, which can also be related to the proper cell design and the implementation of highly reproducible and homogeneously coated commercial materials. Exemplarily, the mean cell impedance at 3 A·cm^{-2} is shown in the inset of Fig. 5a. It is noticeable that the polarization processes are very comparable and at 10 bar differential pressure a lower HFR is detectable. This might be explained by the better compression of the anode half-cell and therefore better contact between PTL and CCM due to the higher cathode gas pressure.

Figure 5b shows the current density distribution along the cell segments at several mean current densities during the polarization curve. For all mean current densities, only minor differences between the current density of the 10 segments are noticeable. This demonstrates the very similar contacting of the segments and the small gradient of temperature and gas amount along the channel due to the high water flow rate applied. The error bars show the total measuring error of the time-depending variation of the current density measurement (cell instability) and the mean value of the 12 contacts per segment. The reproducibility of the current density distribution measurement is given in the Supplementary Information SI 4 for the 10–1 bar measurement. The difference between the conducted measurements is shown for every measured current

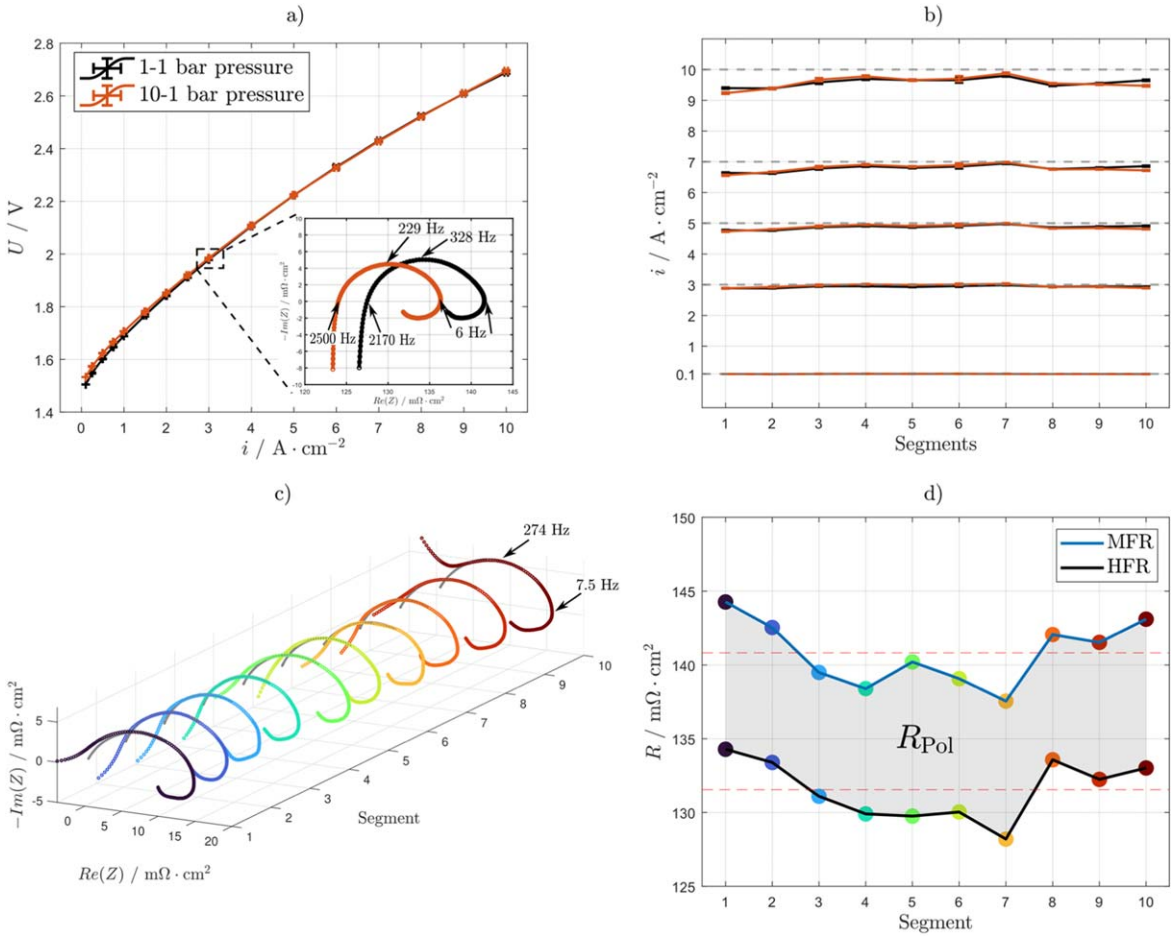

Figure 5. (a) Polarization curve at 1–1 bar and 10–1 bar differential pressure with corresponding impedance spectra at 3 A·cm^{-2} in the inset, (b) current density distribution along the 10 segments at different mean current densities. (c) Locally resolved Ohmic free EIS along the segments at 3 A·cm^{-2} and 10–1 bar differential pressure and (d) evaluation of the HFR, the polarization resistance and the MFR. The measurements are done at 80 °C and a water flow rate at the anode of 20 ml·min^{-1}·cm^{-2} (1200 ml·min^{-1}).

density during the polarization curve with an error of the mean value of all 10 segments being smaller than 1.6%. Additionally, the mean error for the parallel temperature measurement is shown in Fig. SI4a with a value less than 1.2%. SI4b depicts the deviation between the two measurements of current density and temperature distribution of the single segments at 1 A cm^{-2}, 3 A cm^{-2} and 5 A cm^{-2} representative for all current densities.

When comparing the mean value (gray dotted lines) with the distribution of the current densities, two minor trends can be detected: First, there is a small offset between the nominal output of the potentiostat (DC-bias) and the measured current density of the segments, as can easily be seen for the high current densities >5 A cm^{-2} plotted in Fig. 5b. This difference might be assigned to small shunt currents through the complex sense wiring above the PCB at the anode half-cell and the given measurement inaccuracy of ±1%. The different temperatures at the measurement contacts might as well have an influence. The relative difference between the output of the potentiostat and the measured (mean) values using the PCB is linearly increasing with increasing DC-bias. For 0.1 A·cm^{-2} < 1.9% and for 10 A·cm^{-2} < 4.2% relative offset to the output DC-bias is detected for the differential pressure mode.

Second, although only to a small extend, different segments show slightly different values for the mean current densities measured with the PCB. Throughout the numerous measurements performed, these show a random distribution when comparing measurements with different cell assemblies and are therefore assigned to very minor differences in clamping pressure distributions. In the presented case, we find slightly lower local current densities for segments 1, 2 and segment 8, 9 and 10 and slightly higher local current for segment 7. The overall relative standard deviation of the measured mean current densities is for currents ⩾1 A·cm^{-2} < 2% and is constant over the applied DC-bias. The relative measured offset to the potentiostat's output and the relative standard deviation of the segments is shown for all mean current densities in the Supplementary Information SI 6.

Figures 5c and 5d show the impedance spectra along the channel at 3 A·cm^{-2}. The HFR-free locally resolved EIS with the fit for the HFR determination (gray fitting curve at high frequencies, see explanation in Supplementary Information SI 3) is shown in Fig. 5c. Since the current density shows only minimal, statistical fluctuations along the channel, no significant along the channel effects in the EIS are expected and observed. The influence of minor differences in contacting on the polarization resistance is noticeable. At high frequencies the inductive and capacitive artefacts are present but properly circumvented with the high frequency fit of the HFR, see Supplementary Information SI 3. The reproducibility of the impedance measurement is given in the Supplementary Information SI 5 for the mean cell and segment 1, 5 and 10 exemplarily for all segments, as we show the mean value and standard deviation in Bode presentation of the two measurements conducted with two cell assemblies and identical materials used. At high frequencies (>1 kHZ) deviations of the phase angle due to wiring artefacts can be seen. At medium to low frequencies (<1 kHZ) the polarization is very similar with a constant difference in the impedance, which we refer to cell contacting and therefore different values of the HFR. Furthermore, the Kramers Kronig test is done separately for each measurement and shows that both measurements have very low residuals in the low-frequency range but slightly higher errors at high frequencies (>3 kHz) which we refer to wiring artefacts.

Figure 5d shows the HFR fitted with the ECM explained in Supplementary Information SI 3 and the MFR (minimal frequency resistance) which is measured at 100 mHz. The MFR is the impedance value measured closest to the DC resistance. The grey area between HFR and MFR can be described by the polarization resistance (R_{Pol}). The contacting issues can herewith be seen with a random distribution along the channel. The behavior of the impedance along the channel is in very good agreement with the current density measurement. Segments 1, 2, 8, 9 and 10 show

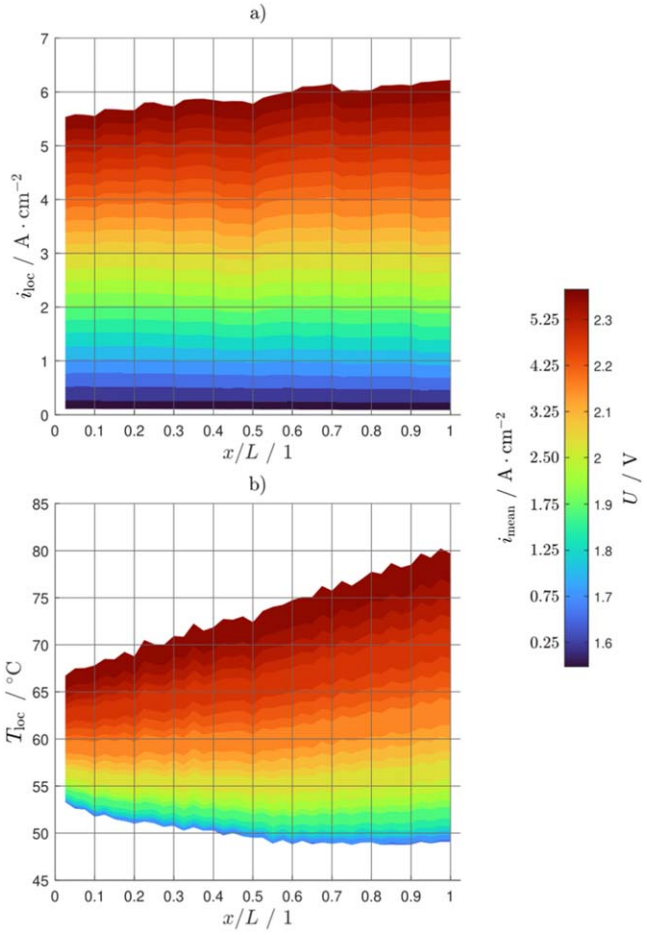

Figure 6. (a) Current density distribution and (b) temperature distribution of the anode flow field plate along the channel during a polarization curve up to 6 A·cm^{-2}. The measurements are done at 60 °C, balanced pressure of 1 bar and a water flow rate at the anode of 2 ml·min^{-1}·cm^{-2} (120 ml·min^{-1}).

relatively high and segment 7 very low HFR and MFR values which is consistent with the trend of the local current densities, see paragraph above.

The results so far demonstrate, that the AtC test cell works very reliably under a broad variety of current densities and pressure settings. Smaller differences in the measured values of the segments are negligible, especially as they can easily be understood and analyzed, e.g. the correlation between the current distribution among the segments and the concomitant EIS. However, locally resolved results at very high current densities (10 A·cm^{-2}) need to be analyzed carefully as the shunt currents circumventing the PCB induce significant deviation from the potentiostat's output.

Figure 6 shows the current density (i_{loc}) and temperature (T_{loc}) distribution measured at the 40 contacts of the middle row of the PCB along the channel during a polarization curve measurement up to 6 A·cm^{-2} at 60 °C water inlet temperature. Purposely, a constant low anode water flow rate of 2 ml·min^{-1}·cm^{-2} (120 ml·min^{-1}) is chosen to see significant gradients along the channel. This flow rate corresponds to a mean cell water stoichiometry of >3800 at 0.1 A·cm^{-2} and ∼64 at 6 A·cm^{-2}. According to the ideal gas law (60 °C, 1 barg pressure), at 6 A·cm^{-2} an oxygen volume fraction of ∼12% at the anode outlet can be predicted.

In Fig. 6a the current density distribution over the 10 segments is quite homogeneous for low mean current densities which is expected due to the good homogeneous contacting of the cell, leading to only small differences in ohmic resistance and the high stoichiometry. Towards higher mean current densities, the local deviations increase.

Since the trend of these differences at a given x/L is the same for all current densities but increases in magnitude with increasing mean current density, we attribute this to initial differences in contacting of the segments. For mean current densities $>4.5\ A{\cdot}cm^{-2}$ a clear increase of the local current density along the channel can be seen.

With a 125 μm thick membrane (Nafion^{TM} N115) that was used for these measurements we face voltages up to 2.37 V at $6\ A{\cdot}cm^{-2}$ and 60 °C which leads to a mean heat dissipation of the reaction of $\sim 5.3\ W{\cdot}cm^{-2}$ (referred to thermoneutral voltage at 60 °C). With the decreasing water content and increasing gas amount, the heat dissipates more through the flow field and the end plates than being removed by the water, which leads to a significant temperature gradient of ∼13 K between inlet and outlet measured via the temperature sensors in the PCB. The water temperature along the channel is increasing even more, 17 K temperature difference were observed between water inlet and outlet under these conditions, measured with the inline temperature sensor in the water-gas stream. At the CCM itself we expect even higher temperatures since the temperature sensors of the PCB are >23 mm (height of flow field plate, see Fig. 1) away from the CCM and a relevant temperature gradient is expected. This explains the increasing current density towards the cell outlet at high current densities.

A membrane dehumidification along the channel would result in an increase of membrane resistance along the channel,[7] which seems not to be dominant for the selected conditions here. The low water flow rate and a stoichiometry of ∼64 seem to create no significant undersupply of water to the catalyst layer and therefore no increasing mass transport resistance. We believe that with today's standard CCM and PTL materials and a proper integration into the cell, undersupply phenomena only occur when operating with extremely low flow rates close to the stoichiometric water amount.

It is to be noted that for low current densities, the heat losses through the end plates are quite high compared to the reaction's heat flux. Therefore, a decreasing temperature is detectable between the cell inlet and center for low current densities. The temperature of the water increases along the channel, which can be seen at the stabilized temperature profile from center to outlet. Change of the heat capacity due to increasing gas amount is negligible due to the tiny amount of gas produced under these conditions. This also explains the different inlet temperatures measured at the anode flow field plate at $x = 0$. The heat flux into the cell (water controlled at the inlet on 60 °C) and the heat exchange surface to the surrounding can be assumed as constant but the reaction's heat changes by a factor of >880 ($\dot{q}_{1.55V} = 0.006\ W{\cdot}cm^{-2}$, $\dot{q}_{2.37V} = 5.296\ W{\cdot}cm^{-2}$) during the polarization curve.

Targeting stack like conditions, any heat transport perpendicular to the flow direction should be avoided in a segmented cell, as in a stack the neighboring cell areas and cells produce similar amounts of heat and the cooling is restricted to the water and the in-plane heat conduction of PTLs and the flow field plate. Thermal insulation or external heating of the end plates could improve the thermal cell behavior which will be considered in future studies.

To analyze the membrane resistance along the channel we compare the HFR at $2\ A{\cdot}cm^{-2}$ and $6\ A{\cdot}cm^{-2}$ along the cell segments, see Fig. 7a.

At $2\ A{\cdot}cm^{-2}$, a temperature difference between inlet and outlet of <1 K is measured and the HFR shows constant behavior along the channel with only small influences by contacting, compare segment 1 and segment 8. This is in alignment with the stable current density distribution shown in Fig. 6a and can be explained by the homogenous temperature profile, the quite homogeneous contacting of the segments and the high stoichiometric water supply of ∼192 at $2\ A{\cdot}cm^{-2}$.

Contrary to this, at $6\ A{\cdot}cm^{-2}$ a temperature difference between inlet and outlet of ∼13 K was measured and a clear decrease of the HFR along the channel is observed, which we refer to the predominant positive temperature and the comparably smaller negative dehumidification influence on the membrane and its conductivity. This explains as well the current density increase along the channel, see Fig. 6a. It is as well remarkable that the mean HFR is lowered by around 15% compared to the measurements at $2\ A{\cdot}cm^{-2}$, which can be explained by the increased mean cell temperature. It is here to be mentioned, that with this study we purposely want to show extreme conditions, knowing that such conditions are not suitable for industrial long-term applications.

Figure 7b shows the comparison of the DC cell resistance R_{DC} given by the slope of the polarization curve shown in Fig. 6 with the locally resolved MFR measured at 100 mHz of the mean cell and exemplarily for the segments at the inlet, center and outlet (segment 1, 5 and 10) over the current density. Since most polarization processes are faster than 100 mHz which corresponds to a time constant of ∼1.6 s, the MFR should be very comparable to R_{DC} if the EIS and the polarization curve are agreeing. R_{DC} is determined by a polynomial fit of the polarization curve and its derivative with respect to the local current density of the segments and the overall current density, respectively.

For the inlet, center, outlet and the mean cell the trend of the MFR and R_{DC} are in good agreement. The difference in magnitude is assigned to the fact that at 100 mHz most but not all processes are included in the impedance measurement. For current densities $>1\ A{\cdot}cm^{-2}$ the MFR shows higher resistance as R_{DC} which is unusual for electrochemical cells but explainable by the inductive loop. Low-frequency inductive loops usually lead to an increase in performance and therefore a decreasing resistance which is partially cut off by not measuring towards 0 Hz. This inductive feature can even lead to the fact that R_{DC} shows lower values than the HFR, which can be seen when comparing Figs. 7a and 7b. This is consistent with the findings of our previous publication on inductive loops.[18] For current densities $<1\ A{\cdot}cm^{-2}$ the inductive loop is not present and therefore only capacitive polarization resistance is detectable, which explains the lower MFR compared to R_{DC} since some slow processes with positive contribution to the cell resistance are not included in the MFR.

The temperature influence is visible when comparing the current densities at segment 1, 5 and 10. At lower (mean) current densities ($<2\ A{\cdot}cm^{-2}$) very comparable resistances and local currents are visible. Towards higher current densities a clear shift of decreasing resistance and increasing local current towards the cell outlet is detected, which is consistent with the HFR distribution analysis, see Fig. 7a. Also, the difference in magnitude between MFR and R_{DC} diverge more when measuring down the channel. As the tendency still seems to have a logical trend for R_{DC} and MFR, we conclude that the low-frequency inductive feature is becoming more relevant towards the cell outlet. The increasing current density along the channel might explain this since the inductive loop is increasing with increasing current density. However, we also think that the harsh conditions at the cell outlet can lead to a higher through-plane temperature gradient, which might increase this feature. The inductive loop is usually increasing with decreasing input temperature, where higher through-plane temperature gradients are expected which might drive this effect. To verify this assumption electrochemical and fluidic modeling is suggested.

For a comprehensive understanding of phenomena occurring along the channel, the presented test cell offers a powerful base. However, the cell shows minor limitations. The fact that the (vertical) distance of the local measurement points to the electrode (>20 mm) is comparably high, which needs to be considered in the temperature measurements since heat dissipation cannot totally be minimized between these two points. With a channel length of 30 cm the cell presents the lower limit of industrial-relevant designs which makes it still possible to be handled in our laboratory. AtC test cells with longer channel length might reveal higher gradients and are even closer to industrial designs. A higher resolution of the impedance measurement, e.g. a segmentation every 1 cm might help to understand poisoning or coating defects for large scale materials which is not the focus of this approach.

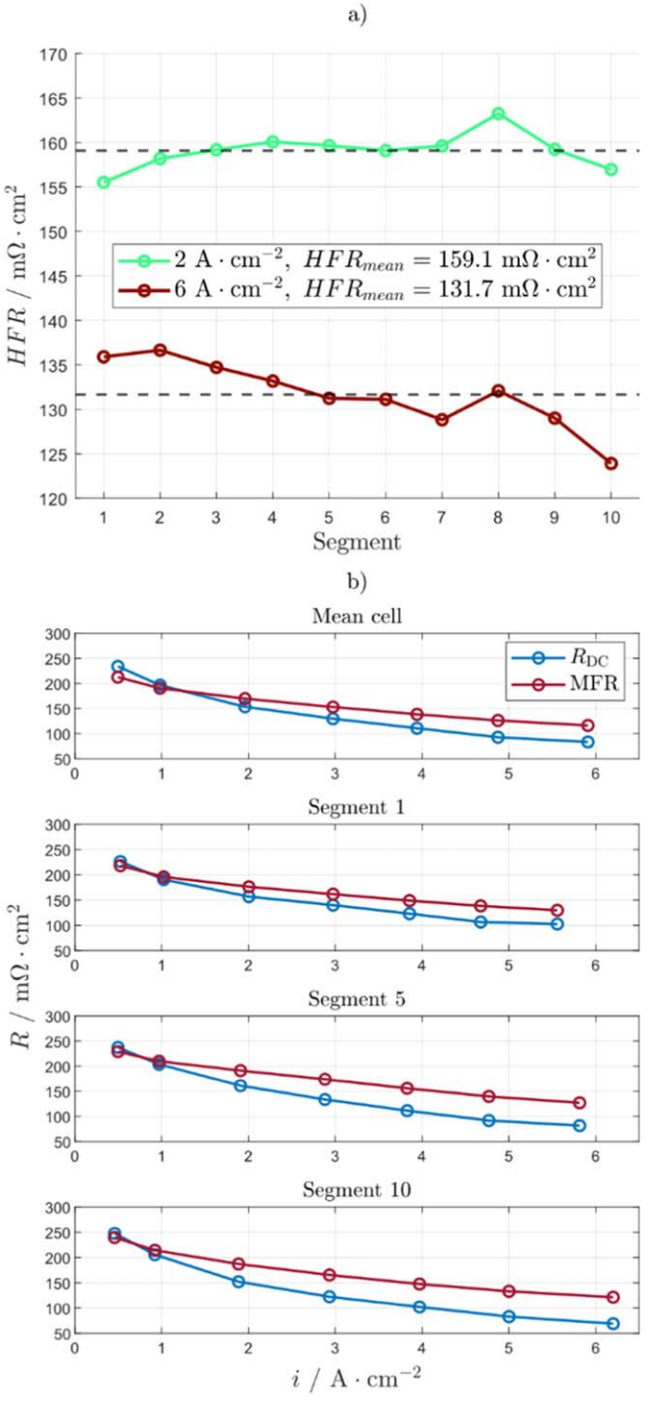

Figure 7. (a) Analysis of the HFR at 2 A·cm^{-2} and 6 A·cm^{-2} along the cell segments and (b) Comparison of the DC resistance and the MFR over the current density of the mean cell and segment 1, 5 and 10. The measurements are done at 60 °C, balanced pressure of 1 bar and of 2 ml·min^{-1}·cm^{-2} (120 ml·min^{-1}).

For future studies. with variations of industrial-relevant operational parameters, locally resolved voltage breakdown and impedance analysis we want to provide more understanding of along the channel phenomena. Furthermore, we will investigate the cell behavior under water starvation and focus membrane and ionomer dry-out and mass transport polarization resistance.

Conclusions

In this work we present a segmented PEM water electrolysis *along the channel* test cell for operation at high current densities up to 10 A·cm^{-2}. The cell is well suited for operating points up to 80 °C and 10 bar differential and balanced pressure. With its 40 contacts along the channel in three rows, highly resolved current density and temperature profiles can be monitored. Due to the possibility of segmenting the flow field plate and the porous transport layer, locally resolved impedance measurements with minimized in-plane crosstalk between the segments can be done in parallel.

Challenges, as the unequal internal contacting of the segments, tightness issues up to 10 bar gas pressure of the segmented bipolar plate and high frequency artefacts in the impedance spectra were faced and have been solved to a suitable level.

It is demonstrated that the locally resolved impedance measurements are in very good agreement with the current density and temperature distribution measurements. Effects of temperature gradients current density, high frequency series resistance and low-frequency impedance response were observable along the channel. Operation up to 10 A·cm^{-2} at 10–1 bar differential pressure could be shown without limitations by the test cell and test bench. However, unequal contacting remains a general issue to be solved within segmented test cells but could be minimized considerably in this setup. The contacting of the segments was optimized to an overall standard deviation of the current density distribution of less than ±5% compared with the mean current density applied, which allows us to properly investigate along the channel effects. Furthermore, we present a method to determine the high frequency series resistance by modeling and extrapolating a specific frequency range in the charge transfer region to circumvent high frequency artefacts due to wiring of the impedance spectra.

For future research, we recommend minimizing the distance between the temperature measurement point to the CCM, which is challenging but might provide more precise information on the temperature dependency of loss processes in the cell. Furthermore, test cells with even longer channels might be closer to large scale industrial applications but challenging regarding the required space in laboratories and test benches. For the impedance analysis a higher resolution combined with voltage measurements in each segment could improve the quality of the measurements.

With the present test cell, we provide a measurement application to close the research gap of industrial-relevant spatially resolved measurements in PEM water electrolysis. Practically, the cell can be used to characterize different materials as flow field channels, PTLs and CCMs along the channel at industrial operation. With the combination of current density, temperature and impedance distribution measurements the analysis of the high frequency resistance and polarization processes can properly be done and essential understanding can be provided.

Acknowledgments

The authors gratefully acknowledge funding from the Federal Ministry of Education and Research, Germany (BMBF, 03HY103F and 03HY103C). We thank Schaeffler Technologies AG & Co. KG, Germany for the collaboration within *H2Giga StacIE*. Our colleagues from the fuel cell characterization and electrolysis group at Fraunhofer ISE as well as Hunter Simonson and Guido Bender from NREL, USA are acknowledged for the fruitful discussion on segmented cells and their optimization.

ORCID

Niklas Hensle https://orcid.org/0009-0001-8308-817X
André Weber https://orcid.org/0000-0003-1744-3732

References

1. J. van der Merwe, K. Uren, G. van Schoor, and D. Bessarabov, "Characterisation tools development for PEM electrolysers." *Int. J. Hydrogen Energy*, **39**, 14212 (2014).
2. B. Verdin, F. Fouda-Onana, S. Germe, G. Serre, P. A. Jacques, and P. Millet, "Operando current mapping on PEM water electrolysis cells. Influence of mechanical stress." *Int. J. Hydrogen Energy*, **42**, 25848 (2017).
3. S. Sun et al., "Behaviors of a proton exchange membrane electrolyzer under water starvation." *RSC Adv.*, **5**, 14506 (2015).
4. S. Al Shakhshir, F. Zhou, and S. K. Kær, "On the effect of clamping pressure and methods on the current distribution of a proton exchange membrane water electrolyzer." *ECS Trans.*, **85**, 995 (2018).
5. M. Müller et al., "Water management in membrane electrolysis and options for advanced plants." *Int. J. Hydrogen Energy*, **44**, 10147 (2019).
6. M. S. Thomassen, A. H. Reksten, A. O. Barnett, T. Khoza, and K. Ayers, "Chapter 6 - PEM water electrolysis." *Electrochemical Power Sources: Fundamentals, Systems, and Applications* (Elsevier B.V., Amsterdam, Netherlands) 199–228 (2022).
7. C. Immerz, B. Bensmann, P. Trinke, M. Suermann, and R. Hanke-Rauschenbach, "Local current density and electrochemical impedance measurements within 50 cm single-channel PEM electrolysis cell." *J. Electrochem. Soc.*, **165**, F1292 (2018).
8. C. Immerz et al., "Experimental characterization of inhomogeneity in current density and temperature distribution along a single-channel PEM water electrolysis cell." *Electrochim. Acta*, **260**, 582 (2018).
9. J. Parra-Restrepo et al., "Influence of the porous transport layer properties on the mass and charge transfer in a segmented PEM electrolyzer." *Int. J. Hydrogen Energy*, **45**, 8094 (2020).
10. T. Lickert et al., "On the influence of the anodic porous transport layer on PEM electrolysis performance at high current densities." *Int. J. Hydrogen Energy*, **45**, 6047 (2020).
11. J. K. Lee et al., "Critical current density as a performance indicator for gas-evolving electrochemical devices." *Cell Reports Physical Science*, **2**, 100440 (2021).
12. A. Martin, P. Trinke, B. Bensmann, and R. Hanke-Rauschenbach, "Hydrogen crossover in PEM water electrolysis at current densities up to 10Acm −2." *J. Electrochem. Soc.*, **169**, 94507 (2022).
13. T. Smolinka, *What Do We Need in PEM Water Electrolysis to Achieve Our 2030 Targets: A Review of Key Challenges.*, *Electrolyser Conference*, Berlin (2023).
14. D. Siegmund et al., "Crossing the valley of death: from fundamental to applied research in electrolysis." *JACS Au*, **1**, 527 (2021).
15. T. Schuler, T. J. Schmidt, and F. N. Büchi, "Polymer electrolyte water electrolysis: correlating performance and porous transport layer structure: Part II. Electrochemical performance analysis." *J. Electrochem. Soc.*, **166**, F555 (2019).
16. C. C. Weber, T. Schuler, R. de Bruycker, L. Gubler, F. N. Büchi, and S. de Angelis, "On the role of porous transport layer thickness in polymer electrolyte water electrolysis." *Journal of Power Sources Advances*, **15**, 100095 (2022).
17. C. C. Weber, J. A. Wrubel, L. Gubler, G. Bender, S. de Angelis, and F. N. Büchi, "How the porous transport layer interface affects catalyst utilization and performance in polymer electrolyte water electrolysis." *ACS Appl. Mater. Interfaces*, **15**, 34750 (2023).
18. N. Hensle, D. Brinker, S. Metz, T. Smolinka, and A. Weber, "On the role of inductive loops at low frequencies in PEM electrolysis." *Electrochem. Commun.*, **155**, 107585 (2023).
19. D. Klotz, "Negative capacitance or inductive loop?—A general assessment of a common low frequency impedance feature." *Electrochem. Commun.*, **98**, 58 (2019).
20. J. S. Gnanaraj, R. W. Thompson, S. N. Iaconatti, J. F. DiCarlo, and K. M. Abraham, "Formation and growth of surface films on graphitic anode materials for Li-ion batteries." *Electrochem. Solid-State Lett.*, **8**, A128 (2005).
21. C. Gerling, M. Hanauer, U. Berner, and K. A. Friedrich, "Experimental and numerical investigation of the low-frequency inductive features in differential PEMFCs: ionomer humidification and platinum oxide effects." *J. Electrochem. Soc.*, **170**, 14504 (2023).
22. K. Chen, N. Ai, and S. P. Jiang, "Origin of low frequency inductive impedance loops of O 2 reduction reaction of solid oxide fuel cells." *Solid State Ionics*, **291**, 33 (2016).
23. A. Schiefer, M. Heinzmann, and A. Weber, "Inductive low-frequency processes in PEMFC-impedance spectra." *Fuel Cells*, **499–506**, 8 (2020).
24. A. Phillips, M. Ulsh, J. Porter, and G. Bender, "Utilizing a segmented fuel cell to study the effects of electrode coating irregularities on PEM fuel cell initial performance." *Fuel Cells*, **17**, 288 (2017).
25. O. Lottin et al., "Experimental results with fuel cell start-up and shut-down. impact of type of carbon for cathode catalyst support." *ECS Trans.*, **69**, 1065 (2015).
26. M. Geske, M. Heuer, G. Heideck, and Z. A. Styczynski, "Current density distribution mapping in PEM fuel cells as an instrument for operational measurements." *Energies*, **3**, 770 (2010).
27. D. Gerteisen, N. Zamel, C. Sadeler, F. Geiger, V. Ludwig, and C. Hebling, "Effect of operating conditions on current density distribution and high frequency resistance in a segmented PEM fuel cell." *Int. J. Hydrogen Energy*, **37**, 7736 (2012).
28. S. J. C. Cleghorn, C. R. Derouin, M. S. Wilson, and S. Gottesfeld, "A printed circuit board approach to measuring current distribution in a fuel cell." *J. Appl. Electrochem.*, **28**, 663 (1998).
29. D. J. Brett, S. Atkins, N. P. Brandon, V. Vesovic, N. Vasileiadis, and A. R. Kucernak, "Measurement of the current distribution along a single flow channel of a solid polymer fuel cell." *Electrochem. Commun.*, **3**, 628 (2001).
30. I. Alaefour, G. Karimi, K. Jiao, and X. Li, "Measurement of current distribution in a proton exchange membrane fuel cell with various flow arrangements—a parametric study." *Appl. Energy*, **93**, 80 (2012).
31. T. Schmitt, R. Bligny, G. Maranzana, J. Dillet, and U. Sauter, "An experimental study of humidity distribution dynamics in a segmented PEM fuel cell." *J. Electrochem. Soc.*, **169**, 124505 (2022).
32. A. Lamibrac et al., "Experimental characterization of internal currents during the start-up of a proton exchange membrane fuel cell." *J. Power Sources*, **196**, 9451 (2011).
33. T. Schmitt, R. Bligny, G. Maranzana, and U. Sauter, "Rapid and local EIS on a segmented fuel cell: a new method for spatial and temporal resolution." *J. Electrochem. Soc.*, **169**, 94504 (2022).
34. I. Dedigama et al., "Current density mapping and optical flow visualisation of a polymer electrolyte membrane water electrolyser." *J. Power Sources*, **265**, 97 (2014).
35. D. Gerteisen, "Realising a reference electrode in a polymer electrolyte fuel cell by laser ablation." *J. Appl. Electrochem.*, **37**, 1447 (2007).
36. Zahner-Elektrik GmbH & Co. KG. Electronic Load EL1002 (Operation Manual); 2024 (July 29, 2024)47.
37. M. Schönleber, D. Klotz, and E. Ivers-Tiffée, "A method for improving the robustness of linear Kramers-Kronig validity tests." *Electrochim. Acta*, **131**, 20 (2014).
38. T. Lickert et al., "Advances in benchmarking and round robin testing for PEM water electrolysis: Reference protocol and hardware." *Appl. Energy*, **352**, 121898 (2023).
39. A. Nouri-Khorasani, E. Tabu Ojong, T. Smolinka, and D. P. Wilkinson, "Model of oxygen bubbles and performance impact in the porous transport layer of PEM water electrolysis cells." *Int. J. Hydrogen Energy*, **42**, 28665 (2017).
40. M. Suermann, T. J. Schmidt, and F. N. Büchi, "Cell performance determining parameters in high pressure water electrolysis." *Electrochim. Acta*, **211**, 989 (2016).